Materials & Design 212 (2021) 110213

Contents lists available at ScienceDirect

Materials & Design

journal homepage: www.elsevier.com/locate/matdes

Design and manufacturing optimization of epoxy-based adhesive specimens for multiaxial tests

Michael Wentingmann [a,*], Nikolas Manousides [a], Alexandros Antoniou [b], Claudio Balzani [a]

[a] Leibniz University Hannover, Institute for Wind Energy Systems, Appelstrasse 9A, 30167 Hannover, Germany
[b] Fraunhofer Institute for Wind Energy Systems IWES, Am Seedeich 45, 27572 Bremerhaven, Germany

HIGHLIGHTS

- Finite Element based specimen geometry optimization resulted in smooth stress distributions and reduced measurement uncertainties of material properties.
- Combining vacuum speed mixing and 3D printed mold inserts led to low porosity specimens, which was verified with μCT scanning.
- Machine-mixed specimens showed ductile behavior while hand-mixed specimens were rather brittle.
- Applied optimizations significantly reduced scatter in all measured material properties and increased strength and strain to failure.

GRAPHICAL ABSTRACT

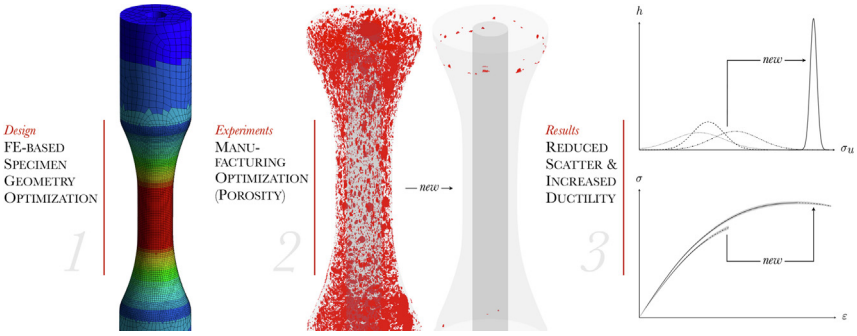

ARTICLE INFO

Article history:
Received 23 July 2021
Revised 11 October 2021
Accepted 31 October 2021
Available online 02 November 2021

Keywords:
Structural adhesives
Multiaxial testing
Porosity analysis
Wind turbine rotor blades

ABSTRACT

Specimen design and manufacturing quality are decisive factors in the experimental determination of material properties, because they can only be reliably determined if all undesired influences have been minimized or are precisely known. The manufacture of specimens from highly viscous, two-component and fiber-reinforced structural adhesives presents a challenge from this point of view. Therefore, a design and manufacturing optimization procedure for fiber-reinforced structural adhesives and multiaxial testing was developed. It incorporated a finite element parametric study to minimize stress concentrations in the specimen geometry. Vacuum speed mixing was combined with 3D printed mold inserts to enable the manufacture of homogeneous specimens with negligible porosity. The method was demonstrated by means of a structural adhesive used to manufacture wind turbine rotor blades, while the manufacturing quality was verified with high-resolution X-ray microscopy (μCT scanning), enabling detailed detection of pores and geometrical imperfections. The results of uniaxial and biaxial static tests show maximized strength and stiffness properties, while the scatter was minimized in comparison to that stated in international literature. A comparison of the mechanical properties and associated manufacturing techniques is given. The comparison includes a porosity analysis of a specimen from an industrial dosing machine used for rotor blade manufacture.

© 2021 The Author(s). Published by Elsevier Ltd. This is an open access article under the CC BY license (http://creativecommons.org/licenses/by/4.0/).

* Corresponding author.
E-mail address: research@iwes.uni-hannover.de (M. Wentingmann).

https://doi.org/10.1016/j.matdes.2021.110213
0264-1275/© 2021 The Author(s). Published by Elsevier Ltd.
This is an open access article under the CC BY license (http://creativecommons.org/licenses/by/4.0/).

1. Introduction

Complex multiaxial loads arise in a variety of engineering disciplines, most of which use structural adhesives in joining processes. To ensure the safe operation of these systems, it is therefore necessary to evaluate the performance of structural adhesives in multiaxial load scenarios.

1.1. Bond lines in wind turbine rotor blades

Among the fields of application of structural adhesives, the wind energy industry in particular is confronted with big challenges in the manufacture of rotor blades. In the manufacturing process of a typical rotor blade, the aerodynamic shells and shear webs are manufactured separately and adhesively joined. Owing to economic constraints and the size of the separate parts, the adhesive also serves as a compensation for manufacturing tolerances. Hence bond lines with a thickness of 10 to 15 mm are usual, depending on the radial and chordwise position [7,19,24,29].

In addition, rotor blades of wind turbines have to withstand high multiaxial loads within their expected lifetime of 20 years. The multiaxiality results from the stochastic wind load in the flapwise direction, which is superimposed with gravitational edgewise loads caused by the rotation of the rotor.

To take account of these loads and manufacturing conditions, adhesives have been developed especially to meet the requirements of the wind energy industry. These adhesives are usually two-component, epoxy-based adhesives with high viscosity. Some are short fiber-reinforced to improve the material properties, e.g., the fatigue performance and cohesive strength [13].

As large quantities need to be applied in a short period of time, the mixing and application process is performed using dosing and dispensing machines [29]. Subsequent to the adhesive application, the shear webs are installed with special positioning equipment and the aerodynamic shells are joined using hinged mold setups, for example. Previously applied surplus adhesive is pushed inward and outward of the targeted bonding location in these production steps.

1.2. State of the art specimen manufacture

In recent publications dealing with rotor blade adhesives, the mixing process used in the specimen manufacture has been simplified and done manually [24,25,35]. This leads to inhomogeneous mixing results and higher levels of porosity, which in turn diminish the mechanical properties of the cured adhesive.

This trend may be amplified during the mold injection process as the injection speed, injection position, mold geometry, vents, etc., can all contribute to the formation of air traps and therefore might increase the levels of porosity and the inhomogeneities. In [11], the presence of voids was attributed to manual pouring and casting, as voids also occurred in specimens, which were mixed in degassed conditions. The specimens in [9] also exhibited high levels of porosity, however, the manufacturing methods used for mixing and mold injection are not clearly specified, therefore hand-mixing seems likely.

This gives rise to the question of how the properties derived from these simplified specimens represent the industrial mixing quality of rotor blade manufacturing and also the associated mechanical properties. This is especially important for multiaxial bulk adhesive specimens, which are particularly challenging to manufacture. However, due to the multiaxiality of the loads of a rotor blade, cf. Section 1.1, multiaxial bulk specimens are required to analyze the cohesive properties in complex loading conditions.

1.3. Aims and outline

To identify material properties unaffected by porosities or inhomogeneities, this work focuses on the geometry and manufacturing optimization of specimens suitable for multiaxial tests. While the motivation for this work is based on wind energy applications, the developed methodology and results have multidisciplinary applicability.

Section 2 summarizes the finite element-based geometry optimization of the specimen. In Section 3, the manufacturing optimization steps are explained. The resulting specimen quality is discussed in Section 4, and the results of the uniaxial and biaxial static experiments are shown and compared to international literature in Section 5. In Section 6, the specimen quality in this work is compared to a specimen from an industrial dosing and dispensing machine used for rotor blade manufacture. The transferability of the laboratory material characterization to the rotorblade manufacturing process is discussed.

2. Specimen design optimization

Several specimen geometries and test configurations are available in the literature for multiaxial tests, e.g., plates [12,26], cruciform types [8,16,27], and tubes [9,30,35]. In general, tubular specimens are described as being most versatile, mainly because multiaxial loads can be applied via arbitrary combinations of normal forces and torsion. The load state can also be proportional or non-proportional depending on the phase shift of the normal and torsional loads. In addition, tubular specimens do not require special load frames, demonstrating enhanced compatibility with testing machinery.

Owing to the aforementioned reasons, the specimen design in this work was chosen to be tubular.

2.1. Optimization objectives

To reliably determine material properties, the following objectives should be met:

1. minimize stress concentrations and maximize the probability of failure within the test section (i.e. sufficient tapering required)
2. approximately constant shear stress in the cross section of the test section (i.e. limitation of the maximum wall thickness)
3. the clamping area must withstand the clamping loads (i.e. limitation of the maximum inner radius)
4. the resulting test loads must be reasonable for the testing machine chosen in both static and fatigue operation to avoid control issues at low load levels (i.e. limitations of the inner radius and the minimum wall thickness)
5. the specimen must not buckle (i.e. limitations of specimen height and wall thickness)

The first objective can be met in a finite element parametric study comparing the maximum equivalent stress in the tapered and clamping section $\boldsymbol{\sigma}_{outer}$ with that of the test section $\boldsymbol{\sigma}_{test}$, leading to the definition of a stress ratio α given by

$$\alpha = \frac{\boldsymbol{\sigma}_{outer}}{\boldsymbol{\sigma}_{test}}. \tag{1}$$

The stress ratio needs to be smaller than 1.

Objectives 2–4 can be fulfilled by setting proper boundary conditions. Objective 5 can only be realized by means of a linear buckling analysis, since a non-linear analysis requires too much computational time for several thousand design variations (design points). Fig. 1 visualizes the design parameters used for this study.

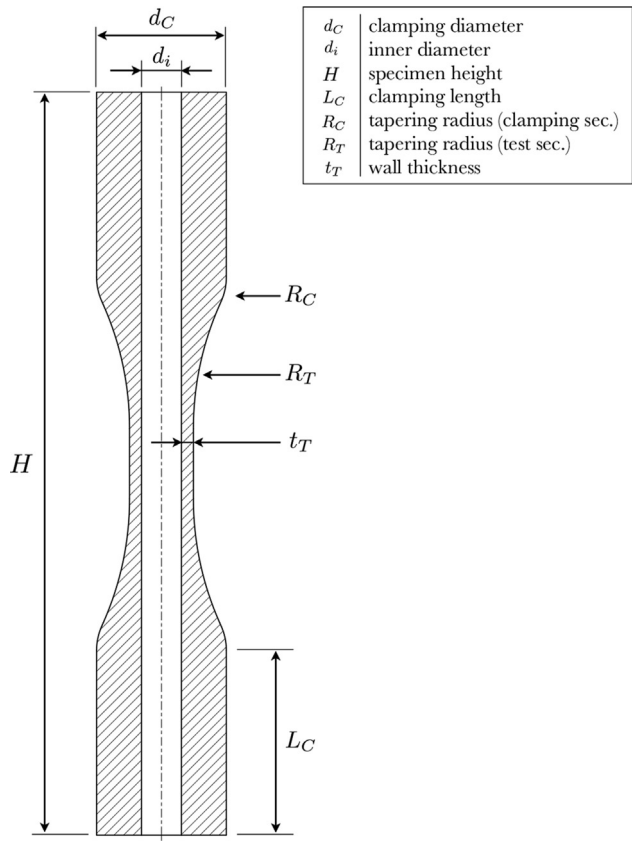

Fig. 1. Specimen design parameters for the finite element parametric study.

2.2. Boundary conditions

The clamping diameter d_C and clamping length L_C are specified by the testing machine. For this study, a servohydraulic Walter + Bai LFV 100-T2000 with cylindrical specimen grips was used. The machine has independent control circuits for axial and torsional loads and can therefore be used for multiaxial testing [34]. The cylindrical grips set the clamping diameter of the specimen to d_C = 30 mm and the clamping length to L_C = 43 mm.

The minimum wall thickness t_T was chosen to be 2 mm to ensure that the specimen would not be damaged in the demolding process and to meet objective 4. The maximum wall thickness was limited to 3 mm to account for optimization objective 2.

The maximum inner radius was set to $r_{i,max}$ = 6.5 mm to meet objective 3 with a sufficient safety factor and to allow for a wide range of R_T and R_C.

The overall height of the specimen H was restricted to 185 mm, because at this height the maximum capacity of the vacuum mixer is reached for all parameter combinations, see Section 3.1.

The test section height was fixed to a minimum of 16.5 mm in order to facilitate the application of strain gauges or other kinds of instrumentation.

Parameter combinations which violated any of the aforementioned boundary conditions were discarded. This limited the maximum values for R_C and R_T in order to keep to the specified minimum height of the test and clamping section.

2.3. Adhesive system

For the experimental campaign, the EPIKOTE™ Resin MGS™ BPR 135G3 adhesive system was used in combination with the EPIKURE™ Curing Agent MGS™ BPH 137G. The solvent free system is epoxy-based, glass fiber-reinforced and very common in the wind energy industry. The adhesive shows shear thinning behavior for all available hardeners [13]. More detailed information on the resin/hardener combinations and related shear thinning, glass transition and mechanical behavior can be found in the technical data sheet of the adhesive [13].

The dimensions of the reinforcement fibers are not published. The fiber volume content was estimated at approximately 8–12 % by means of a preliminary μCT-analysis, but further verification is necessary.

2.4. Finite element modelling

The finite element parametric study was set up in Ansys® Mechanical [2] in combination with a parameterized geometry model in Ansys® SpaceClaim [3]. The parameterized geometries were meshed using solid elements with quadratic shape functions (SOLID186 and 187). The element length outside the test and tapering section was chosen to be 3.5 mm. Inside the tapering and test section the element length was reduced to 0.75 mm, resulting in roughly 250,000 nodes on average for the entire mesh. All design points were evaluated assuming isotropic linear elasticity in separate setups for tension, torsion, compression, and linear buckling.

The stiffness properties were adapted from [35]. The global failure criteria of Stassi-D'Alia [28] and Beltrami [4] were employed as both criteria have been used to evaluate rotor blade adhesives elsewhere [9,23,35,36]. In contrast to the maximum distortion criterion formulated by von Mises (Eq. 2 below, which predicts deviatoric failure), the Beltrami criterion (Eq. 3 below) also includes hydrostatic and therefore volumetric failure. This is considered to be valid for polymers in general [5,20] and also for reinforced polymers [14]. In Eqs. 2 and 3, $\sigma_1, \sigma_2, \sigma_3$ denote the principal stresses, while ν is the Poisson ratio. For incompressible materials with a Poisson ratio of 0.5 the Beltrami criterion converges to the von Mises criterion.

$$\sigma_{vM} = \sqrt{\frac{(\sigma_1 - \sigma_2)^2 + (\sigma_2 - \sigma_3)^2 + (\sigma_3 - \sigma_1)^2}{2}} \tag{2}$$

$$\sigma_B = \sqrt{\sigma_1^2 + \sigma_2^2 + \sigma_3^2 - 2\nu(\sigma_1\sigma_2 + \sigma_1\sigma_3 + \sigma_2\sigma_3)} \tag{3}$$

The Stassi-D'Alia criterion is suitable for adhesives since it takes into account the asymmetry of the static strengths in tension and compression. This is expressed by the factor κ, which is the ratio between the compressive and tensile strength, see Eq. 4.

$$\sigma_S = \frac{(\kappa - 1)I_1 + \sqrt{(\kappa - 1)^2 I_1^2 + 4\kappa\sigma_{vM}^2}}{2\kappa} \tag{4}$$

In Eq. 4, I_1 denotes the first invariant of the stress tensor, and σ_{vM} the equivalent stress according to Eq. 2. When the tensile and compressive strengths are equal, κ is equal to 1 and Eq. 4 becomes Eq. 2. Therefore σ_{vM} can be seen as a special case of σ_S. Using the data published in [35] results in a strength ratio factor of $\kappa = 2.03$.

2.5. Sensitivity study

A sensitivity study was conducted to limit the design space. The design space of this study is shown in Table 1. A total of 2631 design points were evaluated, which is fewer than the combinatorics of all parameters predict, because not all parameter combinations result in valid geometry models in compliance with the boundary conditions specified in Section 2.2.

Although the wall thickness and the inner radius showed no clear trend regarding the stress ratio α, the tapering radius R_T

Table 1
Design space for the sensitivity study of the finite element parametric study (2631 evaluable design points in total).

Parameter	min [mm]	incr [mm]	max [mm]
H	–	–	185
t_T	2	0.1	3
r_i	4	0.1	6.5
R_T	38	12	110
R_C	20	4	36

Table 2
Design space for the final evaluation of the finite element parametric study (1430 evaluable design points in total).

Parameter	min [mm]	incr [mm]	max [mm]
H	165	5	185
t_T	2	0.1	3
r_i	4	0.1	6.5
R_T		max. possible value	
R_C		max. possible value	

showed distinct dependencies. With increasing R_T a significant decrease in α was observed, which was within expectations. On the other hand, R_C had no systematic influences on the stress ratio, see Fig. 2.

Nevertheless, R_C is still important when it comes to the mold injection process, where a smooth transition from test to clamping section helps to prevent the formation of air traps, see Section 3.2. Therefore, R_T and R_C were limited to their respective maxima, which depend on the other variables r_i, t, and H. Since a large specimen height H allows for larger values of R_T and R_C, the minimum height was set to 165 mm. The design space for the final evaluation is shown in Table 2.

2.6. Results

The final design and the resulting stress ratios are shown in Table 3. The ratios are just below or equal to the threshold of 1 for each equivalent stress criterion mentioned in Section 2.4.

To be able to compare the final configuration with previously published tubular geometries, those used in [9,35] were analyzed in the same way as the design points of this study. The comparison revealed that both of these specimens show significant stress concentrations at the end of the tapered section. For this comparison, the transition between tapering and test section was smoothed with a radius of 4 mm in both cases, which is big enough to avoid numerical singularities and still small enough to be an accurate geometry approximation.

The predictions of α show different trends for the compression load case. While the Beltrami criterion predicted $\alpha > 1$ for the geometries of [9,35] and therefore failure outside the test section, the Stassi-D'Alia criterion predicted failure within the test section ($\alpha < 1$). This difference originates from the fact that only the latter accounts for the asymmetry of tensile and compressive strengths. Hence, for this linear elastic study, the results of the Beltrami criterion for tension and compression are the same.

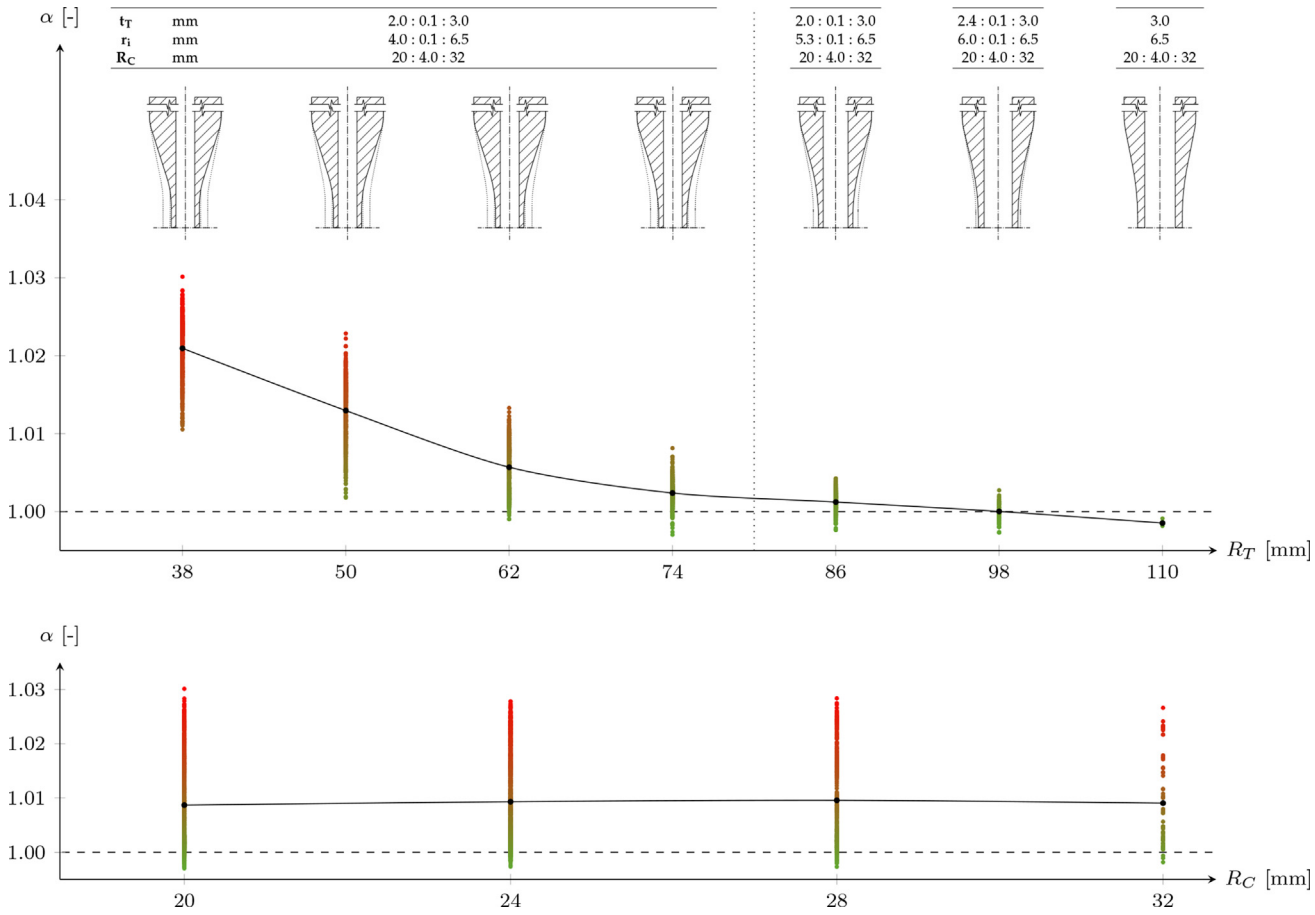

Fig. 2. Results of the sensitivity study for the tensile load case. Stress ratio α versus the tapering radii R_T and R_C. While α decreases for increasing test section tapering radii R_T, the tapering radius towards the clamping section R_C shows no distinct trend. The parameter ranges of t_T, r_i and R_C are shown at the top with corresponding visualizations of the specimen geometry. The parameter ranges are indicated as minimum: increment: maximum.

Table 3
Comparison of the stress ratio α, linear buckling load factor in compression λ, and geometry parameters of the final configuration in this work with previously published multiaxial adhesive specimen designs. The stress distribution for the tensile load case is shown as an example with regions of high stress in red and low stress in blue. * Documented as 0 mm, but set to 4 mm in order to avoid numerical singularities.

Parameter				Zarouchas et al. [35]	Fernandez et al. [9]	This Work
				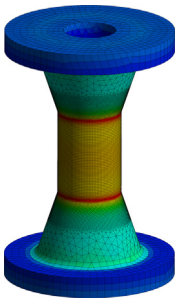	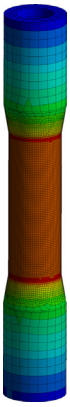	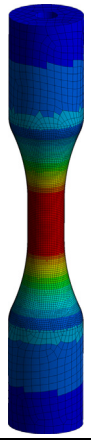
α	Tension	Beltrami	–	1.1189	1.0496	0.9880
		Stassi-D'Alia	–	1.2336	1.1155	0.9961
	Compression	Beltrami	–	1.1189	1.0496	0.9880
		Stassi-D'Alia	–	0.9696	0.9636	0.9776
	Torsion	Beltrami	–	1.0706	1.0433	0.9996
		Stassi-D'Alia	–	1.0707	1.0432	0.9995
λ	lin. buckling load factor (compr.)		–	8.5375	10.5420	8.8439
	Geometry	H	mm	120.0	160.0	175.0
		t_T	mm	2.5	3.0	2.8
		r_i	mm	12.5	7.5	4.7
		R_T	mm	*4.0	*4.0	72.0
		R_C	mm	*4.0	*4.0	14.0

Considering the linear buckling load factors in compression, the geometries used in [35] and this work are approximately equal at $\lambda = 8.54$ and $\lambda = 8.84$, respectively. The geometry used in [9] achieves $\lambda = 10.54$, which is related to a 60 mm distance between the clamping sections instead of 100 mm in the case of [35], and 89 mm in the case of the specimen proposed in this work.

The material properties derived from the optimized specimen in this study should be more reliable, considering that the stress concentrations and measurement uncertainties associated with it were successfully minimized. In terms of buckling, the specimen is expected to act in a comparable way to the specimen in [9,35].

3. Manufacturing optimization

The specimen geometry will only have a significant impact on the experimental campaign if the manufacturing quality is sufficiently high, since local imperfections such as pores also introduce stress concentrations. Therefore, a detailed examination of the manufacturing options and their optimization potential was carried out.

3.1. Optimal mixing quality

To obtain a homogeneous, pore-free mixture, a planetary centrifugal vacuum mixer [32] was used. The operating principle of such a mixer is shown in Fig. 3. The resin and hardener are placed in a mixing container, which spins in an inclined position while at the same time rotating in the normal plane. This generates a whirling motion and mixes the resin with the hardener uniformly within a few minutes.

As the standard mixing containers do not have an outlet suitable for cartridge guns or pumps, the container was replaced with a dosing cartridge. The cartridge chosen was smooth on the inside, so that no stiffeners or other internal structures could disturb the mixing process [22]. It also had a large inner diameter, so that it could be used to mix reasonable amounts of adhesive with good mixing aspect ratios. The mixing aspect ratio is defined as the infill height of the material ($H_{material}$) divided by the diameter of the mixing container ($D_{container}$), Eq. 5.

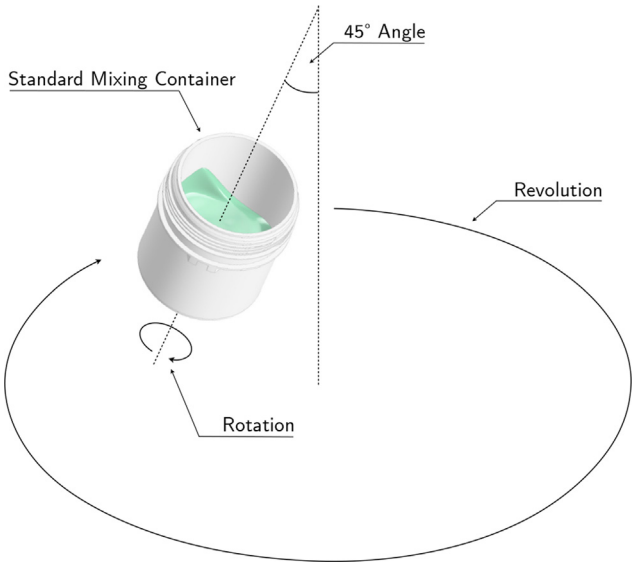

Fig. 3. Mixing procedure of a planetary centrifugal vacuum mixer. The mixture is rotated at an angle, while the container is forced into a revolution in the normal plane.

$$\Lambda_{mix} = \frac{H_{material}}{D_{container}} \tag{5}$$

Incorporating tolerances of the resin and hardener densities and the inner cartridge diameter, the resulting aspect ratio for this study is about $\Lambda_{mix} = 0.7$, which is the upper limit of the recommended range of 0.2 to 0.7. To make the cartridge compatible with the container mount of the mixer, a 3D printed adapter was developed.

To find the optimal mixing parameters, the same mass of adhesive was mixed with nine different mixing parameter settings. The surface temperature was measured with an infrared thermometer (accuracy: ±1.5 °C, resolution: −30 to 500 °C) directly after the mixing process. The mixtures were cured at room temperature and cut along their longitudinal axis. The cured parts were photographed and the mixing quality was evaluated by analyzing the respective rgb-color histograms. Supplementary to the histograms, the multivariate coefficient of variation of the rgb-colors and the number of unique rgb-colors (C_{unique}) were interpreted as a metric of homogeneity. The multivariate coefficient of variation was calculated according to [1], Eq. 6.

$$C_V = \sqrt{\frac{\boldsymbol{\mu}^T \boldsymbol{\Sigma} \boldsymbol{\mu}}{(\boldsymbol{\mu}^T \boldsymbol{\mu})^2}} \tag{6}$$

Therein $\boldsymbol{\mu}$ is the vector of the corresponding mean values and $\boldsymbol{\Sigma}$ is the covariance matrix.

A mixing time of 3 min in combination with a revolution speed of 1500 rpm led to a very homogenous mixture, which was pore-free and reliably reproducible. The surface temperature increased to 40 °C, which is 10 °C more than the recommended conditions stated in the adhesive data sheet [13], but since this rather mild temperature increase only affects the pot life, this was accepted in order to reduce the viscosity, which is expected to help with the mold injection process. Fig. 4 shows an exemplary excerpt of the mixing parameter analysis including the configuration chosen.

3.2. Mold design and injection process

The design of injection molds is an important factor for the overall quality of the specimen, as it impacts the probability that air traps will be created. Two major issues for this study were identified:

1. The tubular specimen design in combination with the chemical shrinkage of the adhesive requires the option to pull or push out the center rod after the curing process.
2. Owing to the high viscosity of the adhesive, it is not possible to pour it into the mold. Instead, it needs to be injected in a continuous motion.

To solve the injection problem, two possible solutions were considered, which are shown in Fig. 5. The first option is to use the center rod itself for the injection. This has the advantage that the flow front is likely to be homogeneous. On the other hand, the center rod cannot be supported at the bottom, so the wall thickness has to be large enough to maintain sufficient stiffness in order to hold the centered position during the injection process. A small inner diameter of the rod combined with large lengths and a high viscosity of the adhesive will lead to very high friction. The hollow rod is also difficult to clean, so that a disposable hose is required inside it, further decreasing the injection diameter and increasing the friction inside the rod.

The second option is to inject from the side, which solves the friction problem. This also allows the rod to be supported at the bottom of the mold, ensuring that it stays centerd. It also makes it feasible to push the rod out rather than being limited to pulling it out. However, this option will make injection more difficult, because the adhesive will be pushed against the rod, pile up and leave voids at the opposite side.

In order to decide on one of the injection options, both were tested with 3D printed mold setups. As the overall friction of the rod injection option was too high to be overcome by available technical options, the main focus was shifted to disposable, 3D printed mold inserts to homogenize the flow front of the side injection option.

Three different insert design concepts were tested in several iterations. Table 4 shows the different insert designs and the resulting flow fronts of the last design iterations for different time steps. The overall last design iteration (No. 8) led to the formation of a very homogeneous flow front, ensuring the same mixing quality inside the mold as in the cartridge after the mixing process. The homogeneity of the flow front is expected to provide a homogeneous distribution and orientation of the reinforcement fibers of the adhesive. It should be noted that the insert design is directly related to the injection speed due to the shear thinning behavior of the adhesive.

To vent the cartridge in parallel to the injection process, the cartridge piston was perforated, and equipped with a semipermeable

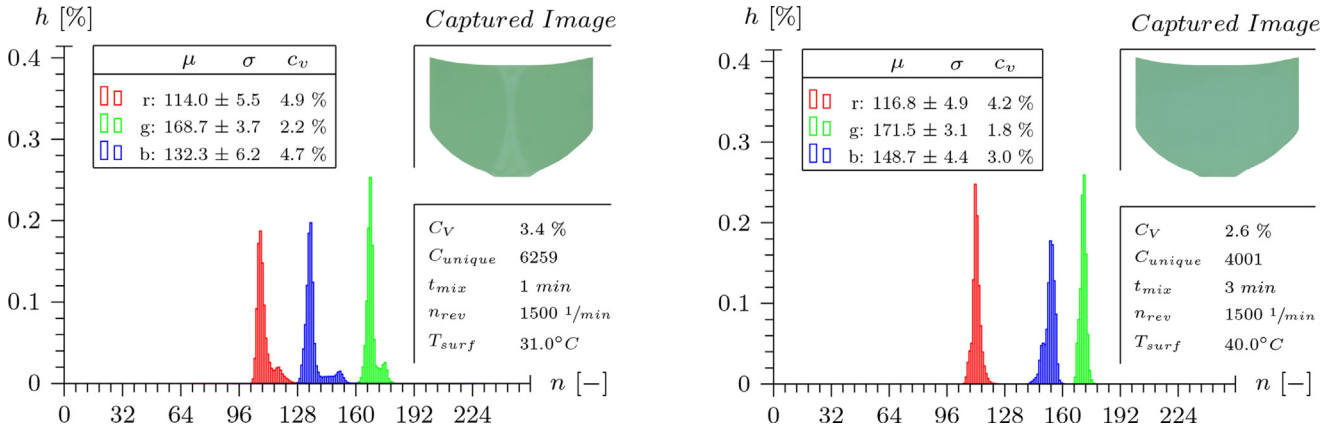

Fig. 4. Result excerpt of the experiments to find the optimal mixing parameters. On the left, the mixing time was too short, leading to an inhomogeneous mixture visualized by brighter colors in the middle of the cured part, as a result of the centrifugal mixing procedure. The final configuration is shown on the right. The rgb-color histograms were analyzed in terms of mean value μ, standard deviation σ, coefficient of variation c_v, multivariate coefficient of variation C_V and unique number of colors C_{unique}. Mixing parameters: mixing time t_{mix}, revolutions per minute n_{rev} and surface temperature T_{surf}.

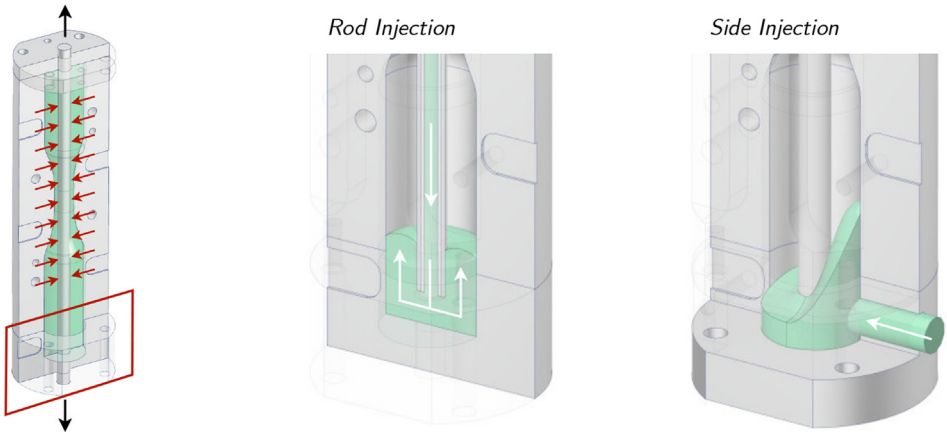

Fig. 5. Injection Options. Rod injection leads to very high friction, but the flow front is likely to be homogeneous. The side injection option introduces less friction, but the adhesive will pile up at the center rod. For both options, the center rod must be pushed or pulled out because of the chemical shrinkage of the adhesive.

Table 4
Mold inserts (3D printed) to homogenize the flow front of the side injection. The upper section shows the different design strategies, while the lower section depicts video snapshots of the injection process at different relative injection times. Insert 8 was chosen as the final design, as it led to a homogeneous flow front which could be reliably reproduced.

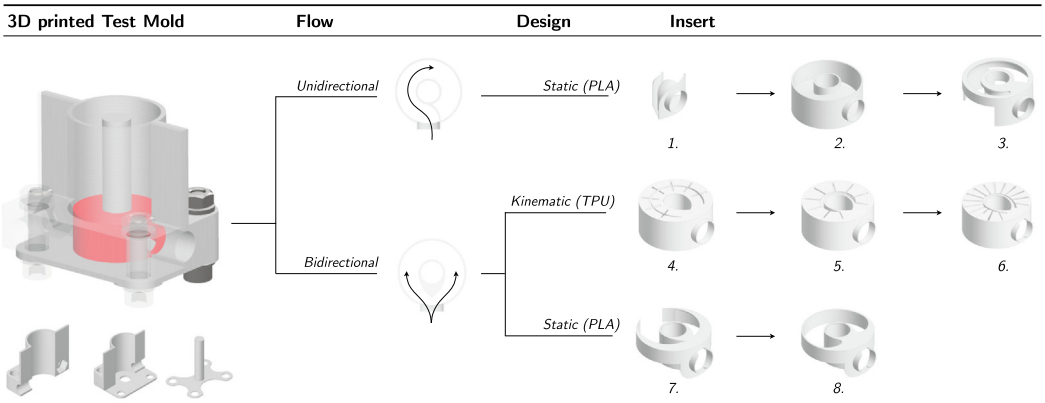

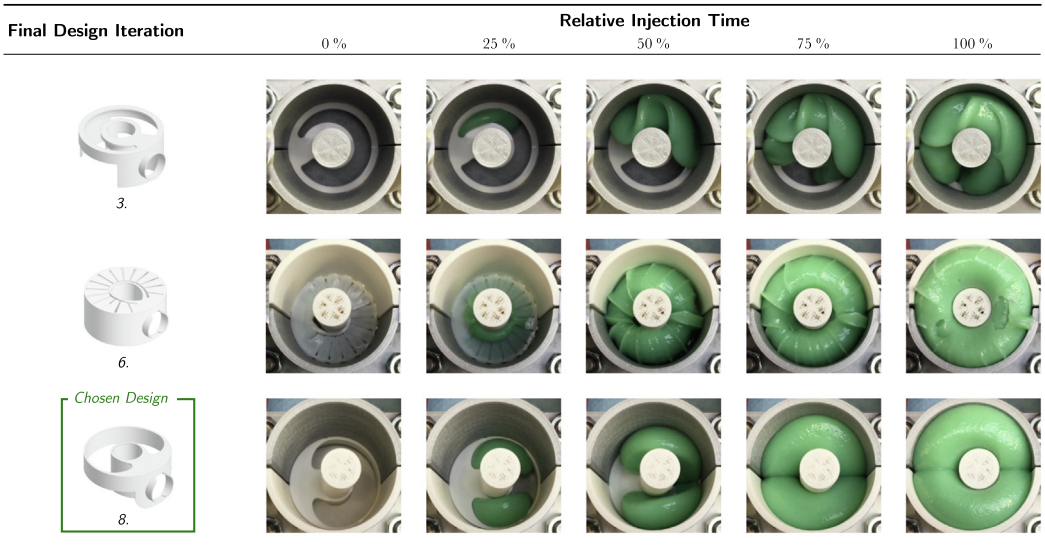

membrane and a 3D printed adapter for an electric cartridge gun to ensure that the piston would not tilt, see Fig. 6. For the cartridge to mold connection, a straight 3D printed nozzle was used to prevent a bent hose causing the formation of air traps.

The final mold design is shown in Fig. 7. The bottom lid needed to be split to be able to demold the specimen including the injection nozzle. The vent was positioned below the top lid and made of four 3D printed polycarbonate parts, which were able to with-

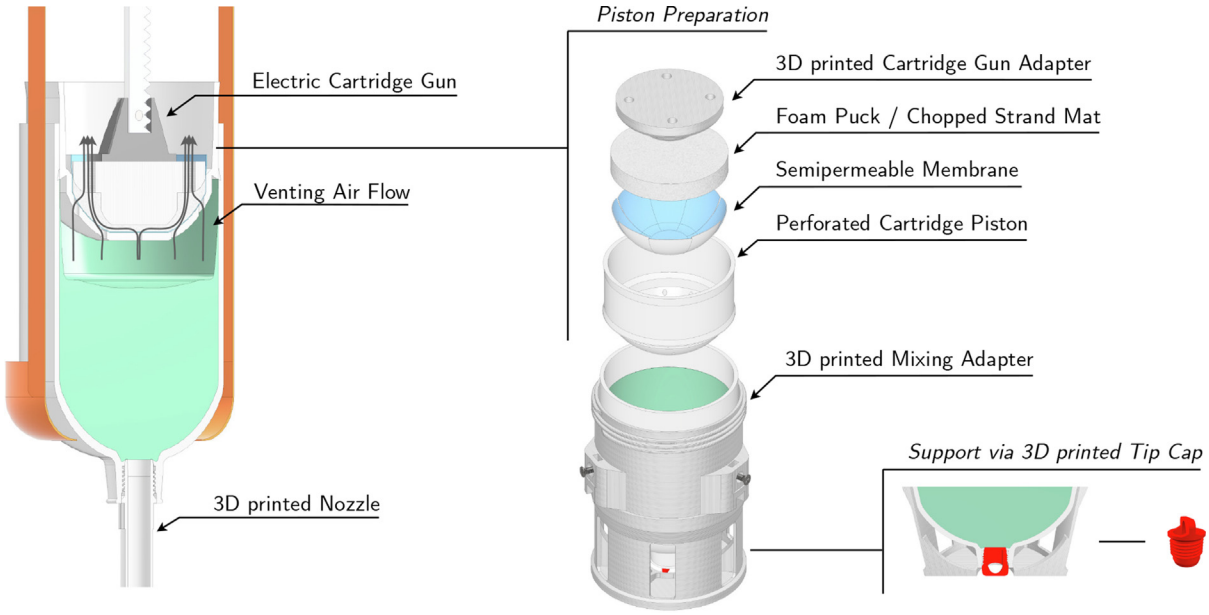

Fig. 6. Cartridge piston preparation to generate a venting airflow in order to prevent the transfer of voids into the mold.

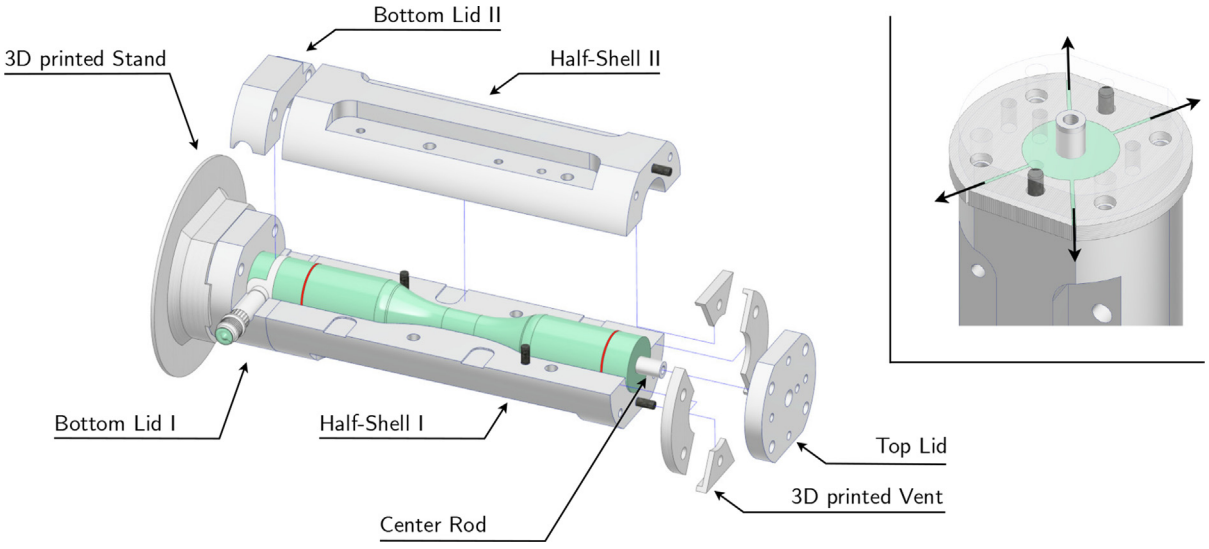

Fig. 7. Final mold configuration. The mold is filled in an upright position. Venting channels are provided by 3D printed parts. The center rod is pressed out of the closed mold with a hydraulic press. The cured specimens are cut at the indicated red lines after demolding.

stand the temperatures present in the tempering process. Similar to the bottom lid, the vent was split to ensure easy demolding, cleaning and reuse.

The upper and lower sections of the mold were extended to be able to cut the areas close to the injection and venting points, so that the final specimen would not be affected by race tracking effects due to a changing flow front in these areas.

4. Quality assurance

To limit unknown influences on the material properties, the manufacturing was documented in detail and examined using high-resolution X-ray microscopy (μCT scanning). It is thus more likely that the scatter of the material properties can be linked to the material itself, rather than being interpreted as the effects of defects.

4.1. Manufacturing performance

In respect of the mixing quality, see Section 3.1, it was possible to precisely adjust the mixing ratio of resin and hardener. The resin and hardener were weighed with a linearity of 50 mg [15], leading to an average mixing ratio (by weight) of 100: 44.99 $\pm$ 0.04. Therefore, it is expected that the mixing ratio is eliminated as a source of uncertainty.

The tempering process was carried out with a programmable oven [18] and controlled with separate temperature sensors inside the molds. Fig. 8 shows the temperature profile of the first specimen production batch (nine specimens). At first, the oven stayed unheated for 6 h to slowly initiate the curing process. The profile defined in the data sheet [13] was set subsequently, and consisted of a 1 °C/min heat-up, 4 h at 75 °C and a 1 °C/min cool-down. The time delay of the adhesive temperature in relation to the oven tem-

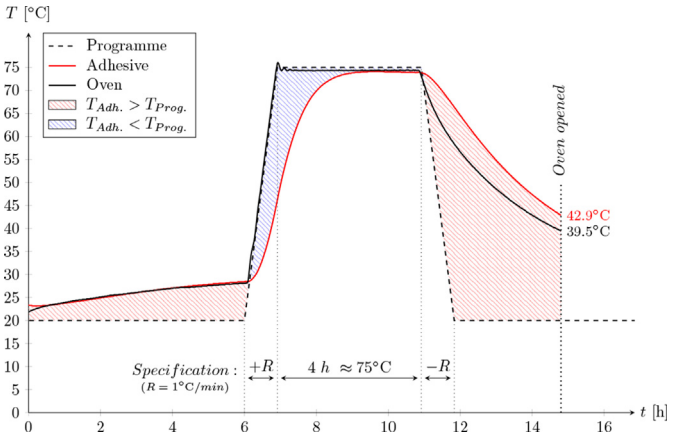

Fig. 8. Exemplary tempering profile for the specimen manufactured. Production batch 1 of 24.

perature led to the adhesive spending less time within the peak temperature regime, but since the oven was not actively cooled there was additional heat flow before the heat-up (exothermal) and during the cool-down (residual heat). The average oven temperature on opening was 34.4 °C.

Humidity and ambient temperature in the accredited laboratory were kept at 50 ± 10 % and 23 ± 2 °C at all times. Influences of varying humidity or ambient temperature on the material properties during storage, manufacture or testing are therefore expected to be negligible.

4.2. High-resolution X-ray evaluation

To check the porosity and geometrical imperfections of the specimens a Zeiss Xradia 410 Versa high-resolution X-ray microscope [6] was used. The scans were limited to the tapered and test section of the specimens to save time, since low levels of porosity in the clamping sections will most likely not affect the specimen performance. Avizo software [31] was used to export convex hull point clouds of the specimens' contour, the center rod and the pores. The post-processing was done in Matlab [17].

In most cases, small pore clusters were found at the end of the upper tapered section, which were generated by slight cross sectional injection speed differences and resulting race tracking effects. At the lower end of the specimens, small pores were detected, that are considered to be the result of race tracking effects within the cartridge at the end of the injection process. However, in both cases the pores were so small that it is very unlikely they have an effect on the material properties measured in the test section.

To verify the impact of the optimizations presented in this paper, three hand-mixed specimens were made in addition to the optimized ones. Table 5 shows the post processed scans of ten optimized specimens and the hand-mixed specimens. While the porosity of the optimized specimens is negligible, the hand-mixed specimens clearly show severe porosity.

The minimal cross sectional areas were extracted from the scan data, further increasing the determination accuracy of the engineering material properties.

5. Uniaxial and biaxial static tests

Uniaxial and biaxial static tests were performed to assess the impact of the optimizations on the material properties of the adhesive.

5.1. Instrumentation

Two strain gauge rosettes were applied to every specimen in diametrically opposite positions to be able to detect and compensate load imbalances. The strain gauges chosen had a low stiffness and self-temperature compensation suitable for epoxy resins [33].

The servohydraulic testing machine [34] used in this study was equipped with a load cell calibrated for class 0.5 to ensure good data quality.

5.2. Uniaxial tests

The tensile tests were performed using the optimized and hand-mixed specimens shown in Table 5. A displacement rate of 1 mm/min was used for both specimen types. Fig. 9 shows the estimated

Table 5
Qualitative porosity comparison of the machine-mixed and hand-mixed specimens from this study. Pores are shown in red. While the machine-mixed specimens have negligible overall porosity and none at all in the test section, hand-mixing results in high levels of porosity throughout the specimens. The specimen numbers are given below the respective depictions.

Optimized (Machine-Mixed) Specimens					Hand-Mixed Specimens		
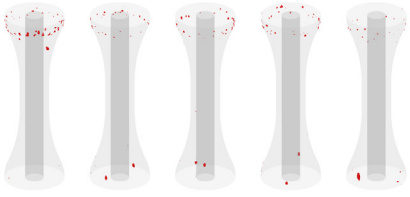					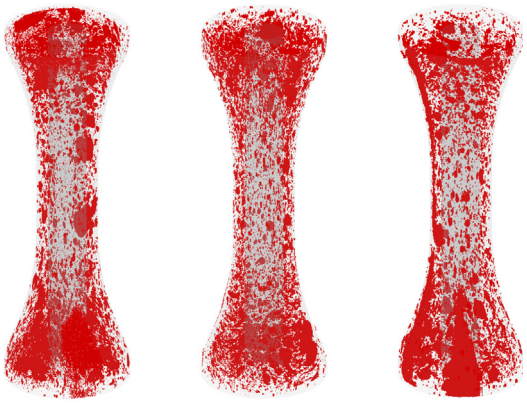		
024	041	048	067	073	204	205	206
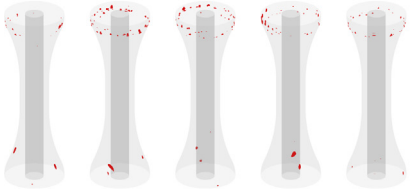							
075	124	132	144	150			

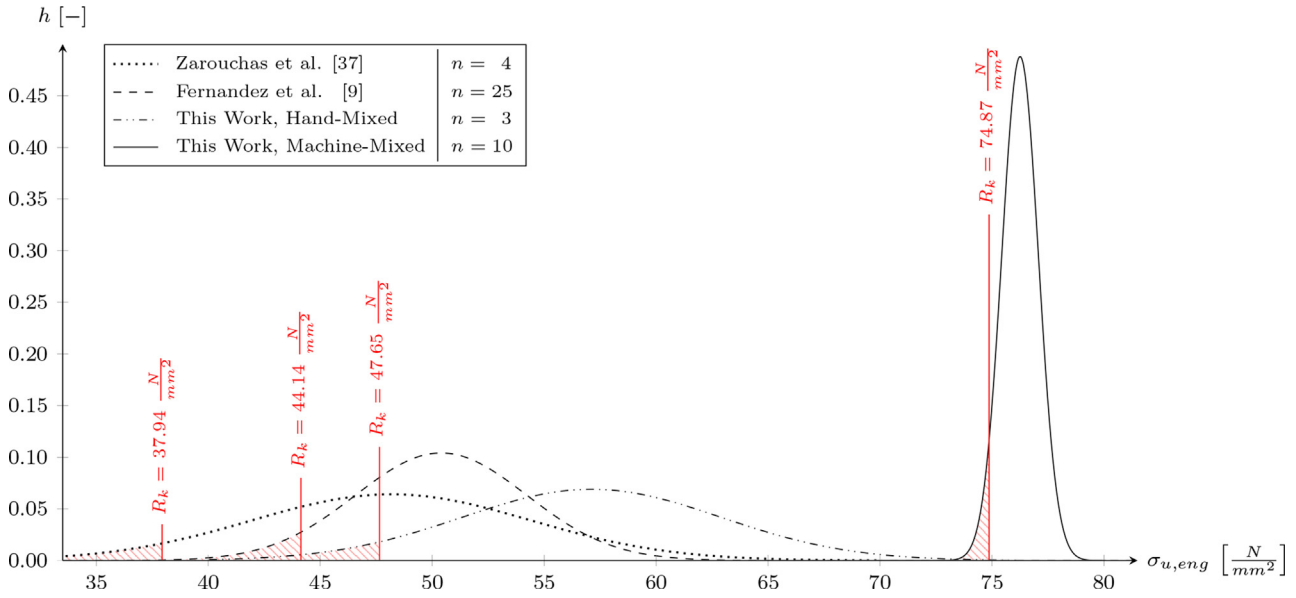

Fig. 9. Estimated frequency distributions of the ultimate engineering tensile strength of Zarouchas et al. [37], Fernandez et al. [9] and this work. Red lines indicate the characteristic strength calculated as the 5th percentile of the frequency distributions, n is the number of specimens. σ_u corresponds to σ_f for all hand-mixed specimens due to brittle behavior (high level of porosity).

frequency distributions of the ultimate engineering tensile stress and the corresponding characteristic strength. The characteristic strength is calculated as the 5th percentile of the estimated frequency distributions. Compared to the results of [9,37], the strength of the optimized specimen is much higher and in good agreement with the strength documented in the data sheet of the adhesive (75 MPa) [13]. In addition, the scatter and therefore the uncertainty is much lower. The same pattern was found for every other mechanical property measured, which is shown in Table 6. The scatter detected is most likely attributable to slight orientation and distribution variations of the reinforcement fibers. Different levels of microporosity, too small to be detected with the scan accuracy used, are also possible, but since the vacuum mixer is very efficient, this is not as likely.

It should be noted that the exact distribution and orientation of the reinforcement fibers is not known. This would require a much higher scan resolution than the one used, which was sufficient to determine porosities and geometrical imperfections. The low scatter seen in the data could therefore be the result of homogeneously chaotic or homogeneously aligned fiber orientations. The latter, anisotropic case seems more likely since the relationship between the elasticity modulus and the shear modulus, Eq. 7, which is valid for isotropic materials, is not valid for the properties derived in this work, see Table 6. An anisotropy is also found for the results of [37]. In [9] the Poisson ratio was not measured, so that the potential degree of anisotropy is unknown.

$$G \neq \frac{E}{2(1+\nu)} \tag{7}$$

The hand-mixed specimens from this work also exhibit a higher strength than the specimens of [9,37], which indicates that the geometry optimization worked well. However, this difference could also arise from an even higher level of porosity in the specimen of [9,37] or may be related to the small number of specimens. Alternating fiber directions could also affect the comparability of the results. The modulus of elasticity of the hand-mixed specimen

Table 6
Comparison of material properties derived from uniaxial tests of bulk tubular specimens. Properties measured in this work were derived by averaging the measurements of the two strain gauge rosettes used to compensate minor load imbalances. Stiffness properties were determined within the strain range of 0.1–0.2 %. The mean value μ, standard deviation σ and coefficient of variance c_v are shown for the tensile failure strength σ_f, tensile failure strain ε_f, modulus of elasticity E, Poisson ratio ν, and shear modulus G.

Parameter	Property	Unit	Adhesive Data Sheet [13]	This Work optimized	This Work hand-mixed	Zarouchas et al. [37]	Fernandez et al. [10]
σ_f	μ	$\frac{N}{mm^2}$	75	76.03	57.12	48.17	50.40
	σ		n/a	± 0.92	± 5.78	± 6.22	± 3.83
	c_v	%	n/a	1.21	10.12	12.92	7.60
ε_f	μ	$\frac{\mu m}{m}$	29000	31399	14084	10228	17900
	σ		n/a	± 2353	± 1585	± 1330	± 3025
	c_v	%	n/a	7.49	11.25	13.00	16.90
E	μ	$\frac{N}{mm^2}$	5500	5711	5315	5412	3928
	σ		n/a	± 56	± 192	± 164	± 503
	c_v	%	n/a	0.97	3.62	3.03	12.80
ν	μ	–	n/a	0.373	0.372	0.398	n/a
	σ		n/a	± 0.005	± 0.016	± 0.013	n/a
	c_v	%	n/a	1.44	4.34	3.28	n/a
G	μ	$\frac{N}{mm^2}$	n/a	1597	n/a	1511	1477
	σ		n/a	± 29	n/a	± 75	± 75
	c_v	%	n/a	1.82	n/a	4.94	5.10

in this work is very close to the results of [37], however. It is thus possible to conclude that the difference in failure strength and strain is likely linked to the stress concentrations and the geometry optimization, respectively.

The averaged engineering stress strain curves of the optimized and hand-mixed specimens in this work are shown in Fig. 10. While the failure strength σ_f of the optimized specimen is 1.33 times higher than that of the hand-mixed ones, the total failure strain ε_f is 2.23 times higher. The plastic strain $\varepsilon_{f,pl}$ increased more than 5-fold. Hence, the porosity difference leads to a brittle material in the hand-mixed case and a ductile material in the machine-mixed case. The stiffness difference was estimated as 7 %. The typical tensile fracture pattern is shown in Fig. 11.

5.3. Biaxial tests

The biaxial tests in this work were performed with displacement control due to the large strains measured in the tensile tests. The displacement rates were adjusted for each axial to torsional load ratio in order to keep the principal strain approximately equal for each ratio at the beginning of the linear elastic section. The effects of different strain rates on ductility and strength were thus minimized. The typical fracture pattern with an initial strain rate ratio of $\dot{\varepsilon}_0/\dot{\gamma}_0 = 1/4$ is shown in Fig. 12.

The failure strengths derived from the biaxial tests are shown in Fig. 13. An ellipsis was fitted to the data set in a non-linear least squares optimization under the assumption that the major axis of the ellipsis coincides with the x-axis. The measurement scatter is indicated by the minimal distance to the ellipsis. As in the case with the tensile tests, it can be observed that the optimized specimens in this work show a higher strength and significantly reduced scatter.

Note that all shear related calculations in [9,35] are based on St. Vernant theory. For the sake of comparison this is adopted in this work and shear stresses are calculated according to Eq. 8.

$$\tau = \frac{T \cdot r_o}{\frac{\pi}{2}\left(r_o^4 - r_i^4\right)} \tag{8}$$

Herein, T is the torque, r_o the outer radius and r_i the inner radius of the test section.

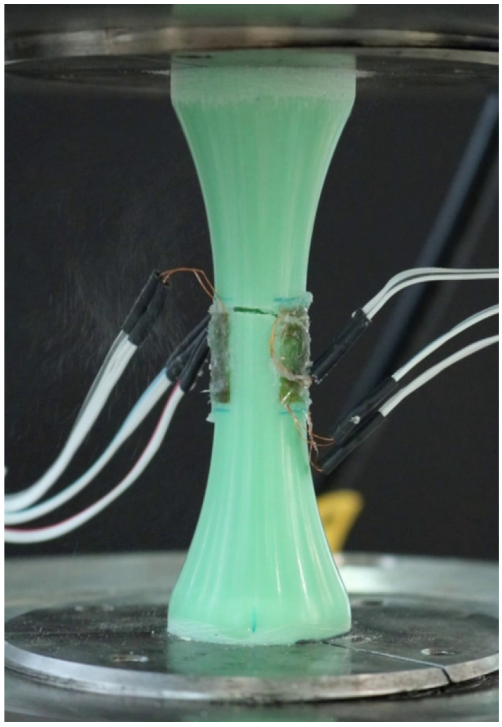

Fig. 11. Typical fracture observed in the tensile tests.

6. Porosity analysis of industrial dosing machines

To enable the comparison of the achievable pore density of the laboratory mixer and an industrial one, cured adhesive inside a conveyor hose of a typical industrial dosing and dispensing machine [21] was analyzed. The processed adhesive was the same system as in this work, see Section 2.3, while 137GF hardener was used instead of 137G. It was assumed that the difference in hardener does not affect the pore density. The cured adhesive inside the hose was μCT-scanned with an accuracy comparable to that used for the tubular specimens in this study.

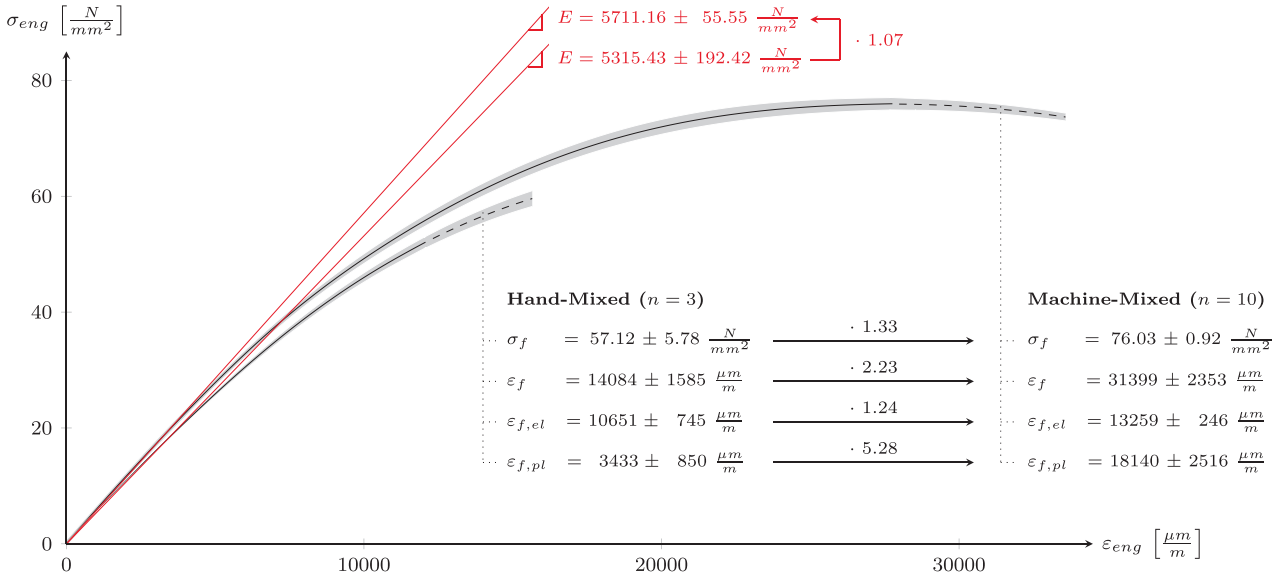

Fig. 10. Averaged engineering stress strain curves of the tensile tests for the machine-mixed and hand-mixed specimens in this work. Gray areas represent the standard deviation of the normal stresses. Dashed lines indicate the range from minimum to maximum failure strain, *n* is the number of specimens.

Fig. 12. Typical fracture observed in the biaxial tests with an initial strain rate ratio of $\dot{\varepsilon}_0/\dot{\gamma}_0 = 1/4$.

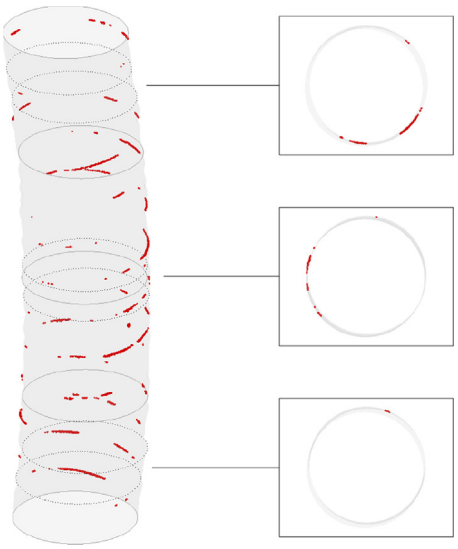

Fig. 14. Qualitative porosity analysis of cured adhesive inside a conveyor hose of an industrial dosing and dispensing machine. The scanned part had a height of 83 mm and an inner diameter of 19 mm (3/4"). The inner contour is shown in gray, pores are highlighted in red. The adhesive is not shown to increase the visibility of the pores.

Fig. 14 shows a 3D depiction and cross sectional views of the inner hose contour and the pores detected. Similar to the machine-mixed specimens in this work, only very small pores were identified, which are probably the result of race tracking effects caused by small ripples on the inner contour of the conveyor hose. The mixing quality in terms of porosity is therefore comparable to that of the manufacturing procedure presented in this work. However, it must be noted that only one specimen from a single dosing machine was analyzed, so that further experimental verification is necessary. It should also be mentioned that large voids can still be present inside the bond lines due to the application process or subsequent manufacturing steps, although the overall porosity might be low.

As shown in Section 5.2, the adhesive exhibits anisotropic behavior due to the reinforcement fibers. Since the orientation of the fibers is dependent on the flow front during the injection pro-

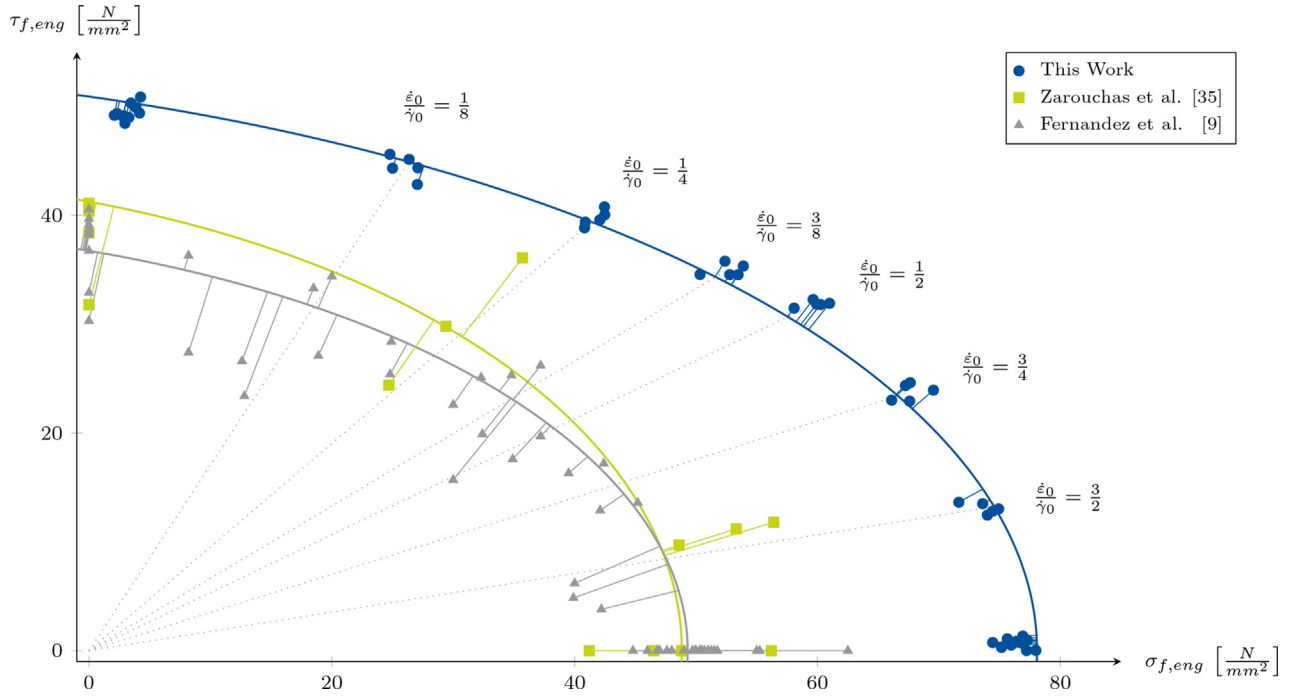

Fig. 13. Comparison of engineering failure stresses of bulk adhesive specimens from this study, Zarouchas et al. [35] and Fernandez et al. [9]. Owing to the high quality of the specimens used in this work, the failure strength is higher than that of the hand-mixed specimens in [9,35]. The initial strain rate ratios shown are only valid for the specimens in this study. Measurement scatter is indicated by the minimal distance to a best-fit ellipsis.

cess on the coupon level, the fiber orientation of rotor blade bond lines will likely also depend on the application process used for the adhesive. Squeezing effects caused by the blade mold closing process mean that the fiber orientation may diverge from the application direction set beforehand by the dosing machine operator. Therefore coupon test results are only generally transferable to rotor blade bond lines if the fiber distributions and orientations are known. Other influencing factors such as the tempering process also affect the transferability of coupon tests. The estimation of in-situ bond line properties therefore remains a challenging task.

7. Conclusion

Multiaxial testing provides the opportunity to test materials and structures in load cases that are close to real world loads of components. However, owing to the more complex test setup, the potential uncertainties associated with these tests are higher than in uniaxial tests. When the material quality is severely affected by the manufacturing processes, e.g., in the case of two-component, fiber-reinforced structural adhesives with high viscosity, the overall uncertainties might be too high to derive reliable material models if the manufacturing is simplified and done manually.

This study therefore focused on the design and manufacturing optimization of specimens made of a fiber-reinforced structural adhesive used for the manufacture of wind turbine rotor blades. The specimen geometry was optimized in a finite element parametric study to avoid stress concentrations. The mixing quality was subsequently optimized using a planetary centrifugal vacuum mixer. To ensure that the mixture was injected into the molds without generating additional porosity and to achieve a homogeneous flow front, 3D printed mold inserts were developed.

The presented optimization procedure is expected to be generally transferable to other types of materials if the mixing parameters and the injection speed are adjusted with respect to the viscosity of the respective material. The limiting factor with high viscosity materials is expected to be the mold injection process and the friction generated therein. The choice of the failure criteria in the finite element optimization might also differ with other materials, although the optimization strategy and objectives stay the same.

High-resolution X-ray tomography was used to check geometrical imperfections and the porosity of the specimens. The scans verified that the porosity of the specimens is negligible. Other effects such as the mixing ratio or the tempering cycle were precisely controlled as well. It is therefore concluded that the optimization presented in this paper enables the determination of material properties unimpeded by manufacturing simplifications.

Owing to the high quality of the specimens, the material properties measured showed significantly less scatter compared to those published in international literature. This is expressed by very low coefficients of variation for strength and stiffness properties of about 1 %. Furthermore, the optimized specimens showed increased failure strength (+33 %), stiffness (+7 %), and failure strain (+123 %) compared to hand-mixed specimens in tensile tests. The measured failure strain difference incorporates a more than 5-fold increase in the plastic strain, so that the machine-mixed specimens can be classified as ductile, while the hand-mixed specimens are more brittle due to their high porosity.

The μCT-analysis of cured adhesive inside a conveyor hose of an industrial dosing and dispensing machine revealed that the mixing quality in terms of the porosity is as low as that of the manufacturing procedure presented in this work. However, the transfer of coupon test results to rotor blade bond lines is only valid if the effects of the distribution and orientation of the reinforcement fibers, as well as all other manufacturing effects on the in- situ characteristics, are known. The fiber orientation inside the specimens in this work is not yet known, but since the flow front within the injection process is very homogeneous, the fibers are likely distributed in the same manner in all the specimens. This is also reflected by the low scatter of the test results. The relationship of the stiffness moduli in tension and shear indicates anisotropic behavior, therefore a certain degree of alignment of the reinforcement fibers seems likely, but further experimental validation is required.

Apart from that, it is expected that the material properties derived from the specimens in this work represent a significantly more accurate material characterization than that obtained from hand-mixed specimens.

CRediT authorship contribution statement

Michael Wentingmann: Implementation of the finite element parametric study, manufacturing optimization, manufacturing and instrumentation of the specimens, execution of the experiments, μCT-scan post-processing, illustrations and writing of the paper. **Nikolas Manousides:** High-resolution X-ray microscopy (μCT scanning) of the specimens and segmentation pre-processing. **Alexandros Antoniou:** Scientific advice and support with executing the experiments at Fraunhofer IWES. **Claudio Balzani:** Conceptual guidance and scientific supervision of all project phases.

Data availability

The raw/processed data required to reproduce these findings cannot be shared at this time due to legal or ethical reasons.

Declaration of Competing Interest

The authors declare that they have no known competing financial interests or personal relationships that could have appeared to influence the work reported in this paper.

Acknowledgements

This work was supported by the German Federal Ministry for Economic Affairs and Energy (BMWi) in the ReliaBlade project (Grant Nos. 0324335A, 0324335B).

References

[1] A. Albert, L. Zhang, A novel definition of the multivariate coefficient of variation, Biometr. J. 52 (2010) 667–675, https://doi.org/10.1002/bimj.201000030.
[2] Ansys®, Mechanical Enterprise, Release 19.2, 2021a.
[3] Ansys®, SpaceClaim, Release 19.2, 2021b.
[4] E. Beltrami, Sulle condizioni di resistenza dei corpi elastici, Il Nuovo Cimento 18 (1885) 145–155, https://doi.org/10.1007/BF02824697.
[5] R.M. Caddell, R.S. Raghava, A.G. Atkins, Pressure dependent yield criteria for polymers, Mater. Sci. Eng. 13 (1974) 113–120, https://doi.org/10.1016/0025-5416(74)90179-7.
[6] A.G. Carl Zeiss, Zeiss Xradia 410 Versa, 2021. https://www.zeiss.com/microscopy/int/products/x-ray-microscopy/zeiss-xradia-410-versa.html.
[7] A.G. Cassano, S. Dev, M. Maiaru, C.J. Hansen, S.E. Stapleton, Cure simulations of thick adhesive bondlines for wind energy applications, J. Appl. Polym. Sci. 138 (2021) 49989, https://doi.org/10.1002/app.49989.
[8] S. Demmerle, J.P. Boehler, Optimal design of biaxial tensile cruciform specimens, J. Mech. Phys. Solids 41 (1993) 143–181, https://doi.org/10.1016/0022-5096(93)90067-P.
[9] G. Fernandez, D. Vandepitte, H. Usabiaga, S. Debruyne, Static and cyclic strength properties of brittle adhesives with porosity, Int. J. Fatigue 117 (2018) 340–351, https://doi.org/10.1016/j.ijfatigue.2018.08.018.
[10] G. Fernandez, D. Vandepitte, H. Usabiaga, B. Van Hooreweder, S. Debruyne, Experimental identification of static and dynamic strength of epoxy based adhesives in high thickness joints, Int. J. Solids Struct. 120 (2017) 292–303, https://doi.org/10.1016/j.ijsolstr.2017.05.012.

[11] A.I.M. Foletti, J.S. Cruz, A.P. Vassilopoulos, Fabrication and curing conditions effects on the fatigue behavior of a structural adhesive, Int. J. Fatigue 139 (2020) 105743, https://doi.org/10.1016/j.ijfatigue.2020.105743.
[12] T.J. George, J. Seidt, M.H.H. Shen, T. Nicholas, C.J. Cross, Development of a novel vibration-based fatigue testing methodology, Int. J. Fatigue 26 (2004) 477–486, https://doi.org/10.1016/j.ijfatigue.2003.10.012.
[13] Hexion™, Technical Data Sheet - EPIKOTE™ Resin MGS™ BPR 135G-Series and EPIKURE™ Curing Agent MGS™ BPH 134G-137GF, 2021.
[14] C.P.R. Hoppel, T.A. Bogetti, J.W. Gillespie, Literature Review-Effects of Hydrostatic Pressure on the Mechanical Behavior of Composite Materials, J. Thermoplast. Compos. Mater. 8 (1995) 375–409, https://doi.org/10.1177/089270579500800403.
[15] Kern & Sohn GmbH, EMB 2000-2, 2021. https://www.kern-sohn.com/shop/en/basic-balances/school-balances/EMB/.
[16] A. Makinde, L. Thibodeau, K.W. Neale, Development of an apparatus for biaxial testing using cruciform specimens, Exp. Mech. 32 (1992) 138–144, https://doi.org/10.1007/BF02324725.
[17] Matlab®, R2020b, 2021.
[18] Memmert GmbH + Co. KG, Universal Oven, 2021. https://www.memmert.com/products/heating-drying-ovens/universal-oven.
[19] P. Noever-Castelos, B. Haller, C. Balzani, Validation of a modelling methodology for wind turbine rotor blades based on a full scale blade test, Wind Energy Sci. Discuss. 2021 (2021) 1–32, https://doi.org/10.5194/wes-2021-24.
[20] K.D. Pae, S.K. Bhateja, The Effects of Hydrostatic Pressure on the Mechanical Behavior of Polymers, J. Macromol. Sci. Part C 13 (1975) 1–75, https://doi.org/10.1080/15321797508068145.
[21] ReliaBlade Project, Increased Reliability of Rotor Blades. Grant numbers 0324335A, 0324335B, 2021. https://www.reliablade.com.
[22] Ritter GmbH, 610 ml Dosing Cartridge. https://www.ritter-cartridges.de/en/products/dosing-cartridges-syringes, 2021.
[23] M. Rosemeier, A. Krimmer, A. Bardenhagen, A. Antoniou, Tunneling Crack Initiation in Trailing-Edge Bond Lines of Wind-Turbine Blades, AIAA J. 57 (2019) 5462–5474, https://doi.org/10.2514/1.J058179.
[24] F. Sayer, A. Antoniou, A. van Wingerde, Investigation of structural bond lines in wind turbine blades by sub-component tests, Int. J. Adhes. Adhes. 37 (2012) 129–135, https://doi.org/10.1016/j.ijadhadh.2012.01.021.
[25] A.T. Sears, D.D. Samborsky, P. Agastra, J.F. Mandell, Fatigue Results and Analysis for Thick Adhesive Notched Lap Shear Test, in: Proc. AIAA SDM Wind Energy Session, 2010. doi: https://doi.org/10.2514/6.2010-2821.
[26] J. Shewchuk, S.Y. Zamrik, J. Marin, Low-cycle Fatigue of 7075–T651 Aluminum Alloy in Biaxial Bending, Exp. Mech. 8 (1968) 504–512, https://doi.org/10.1007/BF02327127.
[27] A. Smits, D. Van Hemelrijck, T.P. Philippidis, A. Cardon, Design of a cruciform specimen for biaxial testing of fibre reinforced composite laminates, Compos. Sci. Technol. 66 (2006) 964–975, https://doi.org/10.1016/j.compscitech.2005.08.011.
[28] F. Stassi-D'Alia, Flow and fracture of materials according to a new limiting condition of yelding, Meccanica 2 (1967) 178–195, https://doi.org/10.1007/BF02128173.
[29] K.P. Subrahmanian, F. Dubouloz, Adhesives for bonding wind turbine blades, Reinf. Plast. 53 (2009) 26–29, https://doi.org/10.1016/S0034-3617(09)70044-X.
[30] G. Tao, Z. Xia, Fatigue behavior of an epoxy polymer subjected to cyclic shear loading, Mater. Sci. Eng. A 486 (2008) 38–44, https://doi.org/10.1016/j.msea.2007.08.044.
[31] Thermo Fisher Scientific, Avizo 2020.2 User Guide, 2020.
[32] Thinky Corporation, Thinky ARV-310 planetary centrifugal vacuum mixer, 2021. https://www.thinkymixer.com/en-gl/products_category/thinkymixer.
[33] Tokyo Measuring Instruments Laboratory Co., Ltd., GFRAB-3-350-50, 2021. https://tml.jp/e/product/strain_gauge/gf_list.html.
[34] Walter + Bai AG, Axial/ Torsional Test Systems, 2021. https://www.walterbai.com/page/products/Materials_Testing_Systems/Combined_Axial-Torsional_Testing_System/index.php.
[35] D. Zarouchas, R. Nijssen, Mechanical behaviour of thick structural adhesives in wind turbine blades under multi-axial loading, J. Adhes. Sci. Technol. 30 (2016) 1413–1429, https://doi.org/10.1080/01694243.2016.1146392.
[36] D.S. Zarouchas, A.A. Makris, F. Sayer, D. Van Hemelrijck, A.M. Van Wingerde, Investigations on the mechanical behavior of a wind rotor blade subcomponent, Compos. Part B: Eng. 43 (2012) 647–654, https://doi.org/10.1016/j.compositesb.2011.10.009.
[37] D.S. Zarouchas, R.P.L. Nijssen, D.R.V. van Delft, Failure analysis of structural adhesives in wind turbine blades under multiaxial loading, in: Proc. DURACOSYS Conference, 2012b.